Structural and Magnetic Study of Order−Disorder Behavior in the Double Perovskites Ba₂Nd₁₋ₓMnₓMoO₆

Fiona C. Coomer[†] and Edmund J. Cussen*

WestCHEM, Department of Pure and Applied Chemistry, University of Strathclyde, 295 Cathedral Street, Glasgow G1 1XL United Kingdom

S *Supporting Information*
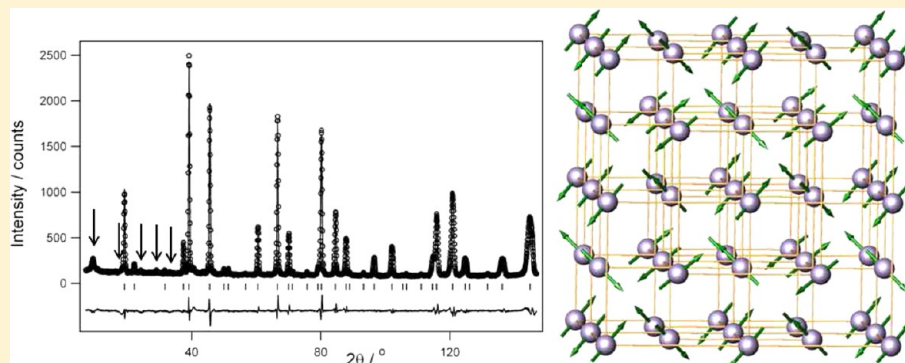
ABSTRACT: The synthesis and structural and magnetic characterization of the site-ordered double perovskites, $Ba_2Nd_{1-x}Mn_xMoO_6$, $0 < x \leq 1$, are reported in order to show the effect of doping Jahn−Teller active, $S = 1/2$, Mo^{5+} into the structure of Ba_2MnMoO_6, which exhibits anomalous long-range antiferromagnetic order. Rietveld refinements against room temperature neutron powder diffraction data indicate that the tetragonal distortion present in the Ba_2NdMoO_6 end member persists to $x \leq 0.3$. This is predominantly manifested as a tilting of the MO_6 octahedra, and there is no evidence of any structural phase transitions on cooling to 1.5 K. For $x > 0.3$, no deviation from the ideal cubic $Fm\bar{3}m$ symmetry is observed. Furthermore, dc-susceptibility measurements confirm that Mn^{2+} is being doped onto the Nd^{3+} site, and the associated oxidation of Mo^{5+} to Mo^{6+}. For all compositions, the Curie−Weiss paramagnetic behavior above 150 K indicates negative Weiss constants that range from −24(2) and −85(2) K. This net antiferromagnetic interaction is weakest when $x \approx 0.5$, where the disorder in cation site occupancy and competition with ferromagnetic interactions is the greatest. Despite these strong antiferromagnetic interactions, there is no evidence in the dc-susceptibility of a bulk cancellation of spins for $x > 0.05$. Low-temperature neutron diffraction measurements indicate that there is no long-range magnetic order for $0.1 \leq x < 0.9$. $Ba_2Nd_{0.10}Mn_{0.90}MoO_6$ exhibits additional Bragg scattering at 2 K, indicative of long-range antiferromagnetic ordering of the Mn^{2+} cations, with a propagation vector $\mathbf{k} = (1/2, 1/2, 1/2)$. The scattering intensities can be modeled using a noncollinear magnetic structure with the Mn^{2+} moments orientated antiferromagnetically along the four different $\langle 111 \rangle$ directions.

■ INTRODUCTION

Electronic degeneracy is associated with a number of interesting and useful physical properties in the solid state. The coupling of the Jahn−Teller instability and magnetic interactions in Mn^{3+} is at the heart of the colossal magnetoresistance in the manganates, $A_{1-x}Ln_xMnO_3$.[1] In these perovskites, the transition metal occupies an approximately octahedral coordination environment that undergoes distortion due to the presence of the doubly degenerate e_g^1 configuration of Mn^{3+}. The mixed oxidation state of the manganese gives a combination of quarter-filled (Mn^{3+}) and empty (Mn^{4+}) e_g orbitals that leads to ferromagnetism that can be partially rationalized as arising from a double exchange interaction.[2]

Electronic degeneracy also arises from partially occupied t_{2g} orbitals, such as those found in Ti^{3+}, 3d t_{2g}^1. The classic example of this is provided by $NaTiO_2$ which contains largely regular octahedral TiO_6 at room temperature but undergoes a Jahn−Teller distortion at ∼220 K.[3] The interaction between the t_{2g} orbitals and the ligand field is considerably weaker than between the e_g orbitals involved in Mn^{3+} or Cu^{2+}, and the Jahn−Teller distortion is observed at a commensurately lower temperature, with a smaller displacement of the oxide anions around the transition metal.

We have been studying a family of perovskites where Mo^{5+}, $4d^1$, occupies half of the octahedral sites in the perovskite structure. The remaining octahedral sites are occupied by lanthanide cations, and due to the difference and in size and charge between Ln^{3+} and Mo^{5+}, this leads to chemical ordering across two crystallographic sites and a doubling of the
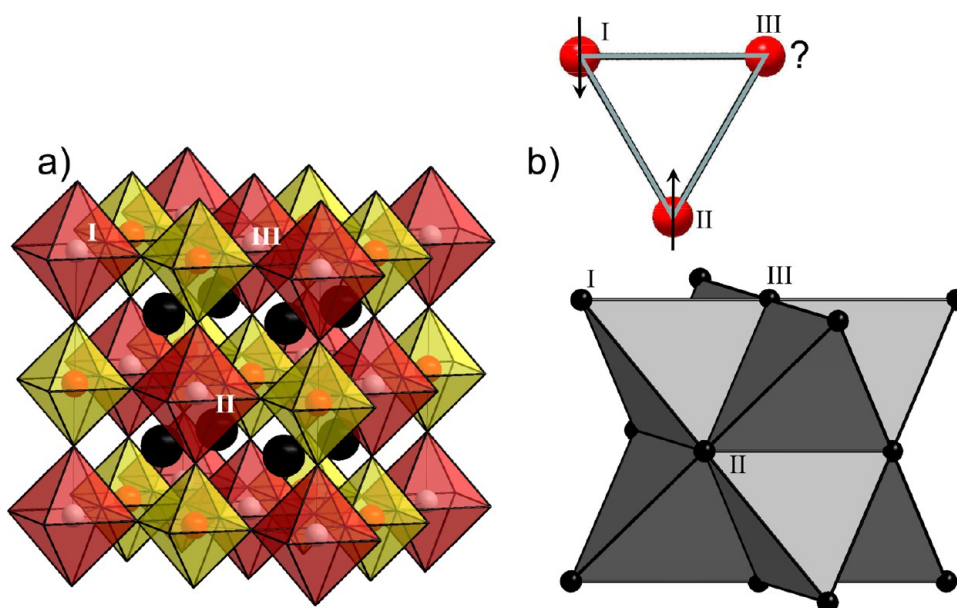
Figure 1. (a) Face-centered cubic lattice exhibited by cation-ordered perovskites from the series $Ba_2Nd_{1-x}Mn_xMoO_6$. Red and yellow polyhedra represent Nd/MnO_6 and MoO_6 octahedra, respectively. (b) shows the lattice points on the *fcc* lattice and illustrates the geometric frustration for three Mn moments on positions labeled as I, II, and III in each diagram.

perovskite lattice parameter to give the face-centered cubic (*fcc*) structure shown in Figure 1. Antiferromagnetic coupling between the points of the *fcc* lattice leads to geometric frustration.[4] This arises as the magnetic centers are arranged on the points of an equilateral triangle to form tetrahedra that are connected through edge sharing, as shown in Figure 1.

The perovskite structure can undergo a large range of structural distortions that reduce the symmetry and so partially remove the magnetic frustration. This combination of frustration and structural variability has led to a range of unusual physical properties in the cation-ordered perovskites Ba_2LnMoO_6.[5−7] For the larger lanthanides, it has been shown that Ba_2SmMoO_6 and Ba_2NdMoO_6 undergo distortion of the MoO_6 octahedra on cooling. Ba_2SmMoO_6 distorts at 353 K to a triclinic phase,[8] whereas Ba_2NdMoO_6 undergoes a gradual distortion of the MoO_6 octahedra while retaining tetragonal symmetry to ~150 K.[9] Below this temperature, Ba_2NdMoO_6 becomes triclinic with a distortion in the Mo^{5+} environment that leads to four short Mo−O distances of 1.96 Å and two longer bonds of 2.00 Å. Both Ba_2SmMoO_6 and Ba_2NdMoO_6 form antiferromagnetically ordered phases where the magnetic structure indicates anisotropic coupling due to the structural distortion.

For smaller lanthanides, these compounds are cubic and provide excellent systems for studying the frustrated magnetism that arises in an antiferromagnetically coupled face-centered lattice.[10] For Ba_2YMoO_6 and Ba_2LuMoO_6, the absence of structural distortion leads to the *fcc* structure giving rise to geometric frustration and prevents the formation of an antiferromagnetically ordered phase.[5,10] Instead, short-range correlations occur leading to partial spin cancellation and unusual behavior such as a valence bond glass in the case of $Ba_{2-x}Sr_xYMoO_6$[5,6,11] and Ba_2LuMoO_6.[12] The cubic compound Ba_2MnMoO_6 contains an arrangement of diamagnetic Mo^{6+} and Mn^{2+} ($S = 5/2$) and antiferromagnetic interactions between Mn^{2+} that occupy the sites of the ideal *fcc* lattice.[13−15]

Structural studies of Ba_2MnMoO_6 suggest no mechanism for lifting this degeneracy of the antiferromagnetic interactions, and

so a long-range ordered antiferromagnetic ground state should not be realized in this phase. However, Ba_2MnMoO_6 is reported to adopt an antiferromagnetically ordered structure with an ordered magnetic moment, ~4 μ_B, that indicates almost complete order below a transition temperature of $T_N \approx 10$ K.[13,14]

As part of a program to investigate the Jahn−Teller activity of Mo^{5+}, we have chosen to examine the effect on Ba_2MnMoO_6 of introducing Mo^{5+} ($S = 1/2$) into the structure via the compositional series $Ba_2Nd_{1-x}Mn_xMoO_6$. This study is designed to illuminate both the origins of the anomalous antiferromagnetism reported for Ba_2MnMoO_6 and the quenching of the Jahn−Teller effect on partial replacement of Mo^{5+} with Mo^{6+}.

■ EXPERIMENTAL SECTION

Polycrystalline samples of $Ba_2Nd_{1-x}Mn_xMoO_6$ ($0 < x \leq 1$) were prepared using conventional solid state reactions from reagents supplied by Alfa Aesar with purities of not less than 99.99%. Stoichiometric quantities of $BaCO_3$, Nd_2O_3 (stored at 800 °C to prevent CO_2 uptake), MnO_2, and MoO_3 were thoroughly ground together and pressed into pellets. Initially, the pellets were heated in air from 500 to 800 °C at 1 °C min^{-1} and held at 800 °C for 8 h, in order to limit volatilisation of molybdenum oxide. After regrinding, the pellets were further heated at 1250 °C in a flow of 5% H_2 in N_2 gas for 48 h to yield black powders. The reaction progress was monitored by X-ray powder diffraction.

X-ray powder diffraction data were collected using a Siemens D500 diffractometer with Cu K_α radiation. Measurements over the range 5° $\leq 2\theta \leq 100°$ with a step size of 0.02° were performed in order to collect data suitable for Rietveld refinement. Neutron diffraction measurements were performed on the high-resolution powder diffractometer D2B at the Institut Laue-Langevin in Grenoble with a neutron wavelength of 1.594 Å. Data were analyzed by Rietveld refinement using the GSAS suite of programs,[16,17] employing a pseudo-Voigt peak shape and a shifted Chebyshev function to model the background.

A Quantum Design MPMS SQUID magnetometer was used to perform *dc*-susceptibility measurements. Polycrystalline samples (~50 mg) were placed into a gelatin capsule and measured after cooling

both in zero applied field (*zfc*) and in an applied field (*fc*) of 1000 G. Measurements were performed in an applied *dc*-field of 1000 G. As is normally the case for strongly magnetic metal oxides, a diamagnetic correction was not applied to these data.

■ RESULTS

Rietveld refinements against X-ray diffraction data indicate that single phase samples were formed across the entire compositional range $Ba_2Nd_{1-x}Mn_xMoO_6$, $0 < x \leq 1$. The data collected from all samples, with the exception of $Ba_2Nd_{0.90}Mn_{0.10}MoO_6$, could be indexed in the space group $Fm\overline{3}m$, indicating cation ordering between Nd/Mn and Mo across the octahedral sites in the structure. The splitting of peaks in the data collected from $Ba_2Nd_{0.90}Mn_{0.10}MoO_6$ necessitated a lowering of the space group symmetry to $I4/m$ in order for a satisfactory agreement to be obtained. This effect is similar to that observed in Ba_2NdMoO_6 and is driven by the size mismatch between the Ba^{2+} cations and the relatively large NdO_6 octahedra.[10]

The high electron density of the metal cations dominates the X-ray diffraction profile; therefore, Rietveld refinement against these X-ray diffraction data do not allow the determination of the oxide positions with meaningful accuracy. This gives large uncertainties in the metal-oxide bond lengths determined using X-ray diffraction. To obtain insightful structural information on these compositions, neutron diffraction data were collected from representative members of the series in order to identify precisely the oxygen displacements.

Neutron diffraction data collected from $Ba_2Nd_{0.90}Mn_{0.10}MoO_6$ at room temperature were fitted using the $I4/m$ space group, with $a = 5.99854(6)$ Å, $c = 8.5304(2)$ Å, $R_{wp} = 3.15$, and $\chi^2 = 3.54$. When the sample was cooled to 1.5 K, no evidence of a structural transition or magnetic Bragg scattering was observed. Initially, the neutron diffraction data from the $x = 0.2$ and 0.3 members of the series were modeled using the $Fm\overline{3}m$ space group determined by X-ray diffraction, as there was no evidence of splitting of high angle peaks to indicate a reduction in symmetry, as shown in Figure 2c. Although all the peak positions were accurately modeled, there was significant discrepancy in the relative intensities of a number of peaks, resulting in a poor fit ($R_{wp} = 2.56$ and $\chi^2 = 5.03$ for $x = 0.2$), as shown in Figure 2a. In order to model this intensity discrepancy, the symmetry was lowered to the tetragonal space group $I4/m$. Although the unit cell parameters remain metrically similar, lowering the symmetry of the space group allows the peak intensities to be more accurately modeled ($R_{wp} = 2.13$ and $\chi^2 = 3.50$ for $x = 0.2$), as shown in Figure 2b, by allowing the rotation of the M-O octahedra about the [001] axis, $a^0a^0c^-$ in Glazer notation.[18] Similarly, reducing the symmetry of the space group used in the refinement of the $x = 0.3$ analogue, results in a better quality fit.

For $Ba_2Nd_{0.50}Mn_{0.50}MoO_6$, the refinement was not stable when the symmetry was reduced to $I4/m$, and there was no improvement in the quality of fit observed in allowing the rotation of the MoO_6 octahedra. On the basis of these neutron diffraction data, we conclude that the compositional series undergoes a structural transition as a function of composition between tetragonal $Ba_2Nd_{0.70}Mn_{0.30}MoO_6$ and cubic $Ba_2Nd_{0.50}Mn_{0.50}MoO_6$. There was no evidence of a reduction in symmetry from the $Fm\overline{3}m$ space group for the remainder of the series ($x \geq 0.5$). The size of the unit cell was found to decrease on increasing the concentration of manganese in the samples, as is expected on decreasing the average size of the *B*-site cation, and the magnitude of the distortion is
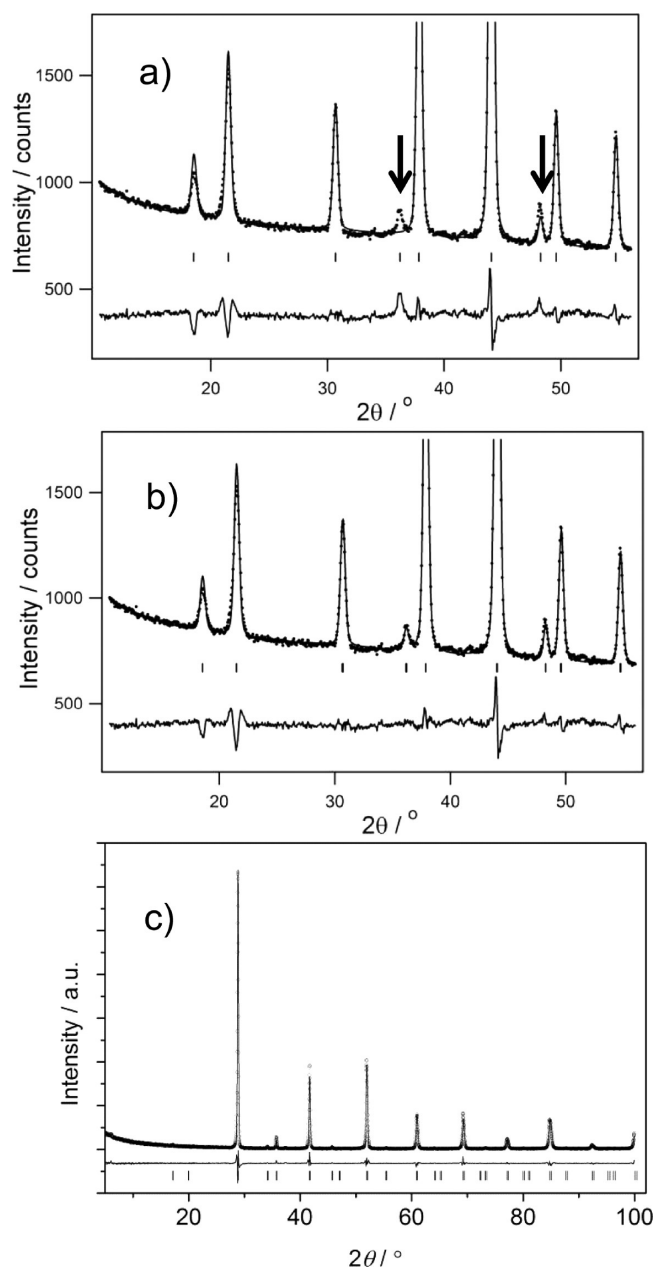
Figure 2. Neutron powder diffraction data collected at room temperature from $Ba_2Nd_{0.80}Mn_{0.20}MoO_6$ and fitted using the space groups (a) $Fm\overline{3}m$ and (b) $I4/m$. The cubic model gives a large intensity mismatch in the subset of peaks as indicated in (a). Fitted X-ray diffraction profile from this compound is shown in (c).

simultaneously progressively reduced. The tilt angle associated with the tetragonal distortion and the lattice parameters are shown in Figure 3.

Trial refinements were used to test for nonstoichiometry by varying the occupancies of the oxide and octahedrally coordinated cation sites. These gave refined compositions that were within 1% of the target stoichiometries, with no detectable cation disorder or vacancies on the oxide sublattice. When cooled to 1.5 K, there was no evidence of any phase change or any indication of the onset of long-range magnetic order for any of the samples for $x < 0.9$. Structural parameters and atomic coordinates are collected in Tables 1 and 2, respectively.
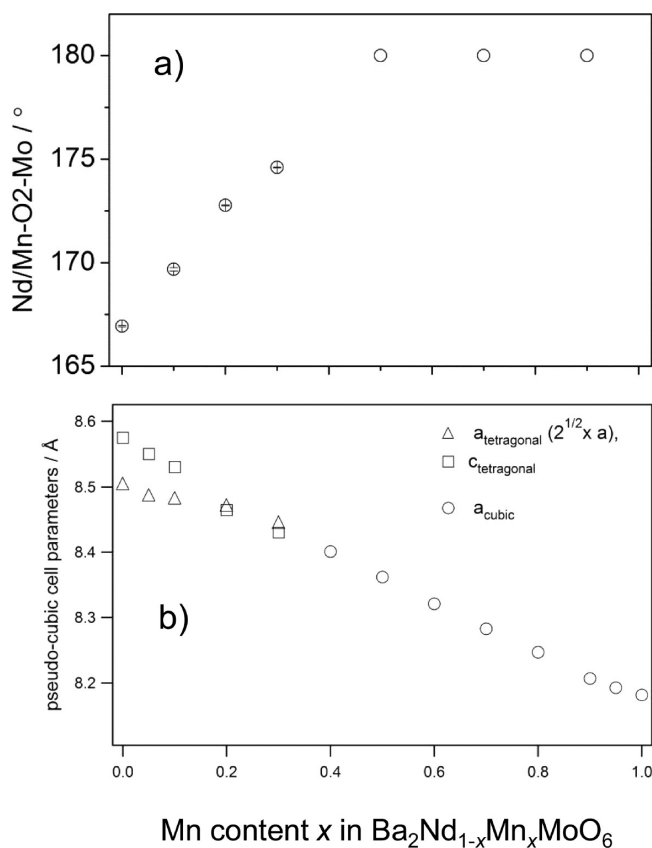
Figure 3. Tetragonal distortion for $x \leq 0.3$ is manifested in the Nd/Mn−O−Mo bond angle shown in (a), derived from neutron diffraction data collected at room temperature. Despite this distortion, the cell is metrically close to cubic in compositions $x \geq 0.2$, as shown in (b). Lattice parameters for the compounds $Ba_2Nd_{1-x}Mn_xMoO_6$ are derived from refinement against room temperature neutron or X-ray powder diffraction data. Estimated standard deviations in the lattice parameters are smaller than the symbols. Values for Ba_2NdMoO_6 and Ba_2MnMoO_6 are taken from the literature.[10,13] For tetragonally distorted compounds ($x \leq 0.3$), the a lattice parameter is expressed as $a\sqrt{2}$ to allow ready comparison with the cubic phases.

Temperature-dependent dc-susceptibility (χ) measurements show that across the entire series there is no separation of zfc and fc-susceptibility and Curie−Weiss behavior is observed above 15 K, as shown in Figure 4. Fitting the data above 150 K gave the Curie−Weiss parameters listed in Table 2, and the temperature dependence of the inverse susceptibility is shown in Figure 5. For $T < 10$ K, a separation of the zfc and fc data is observed across the whole series, accompanied by a deviation from ideal Curie−Weiss behavior. $Ba_2Nd_{0.95}Mn_{0.05}MoO_6$ exhibits a sharp peak in the susceptibility at 11 K similar to that observed in Ba_2NdMoO_6 indicative of long-range antiferromagnetic ordering and a Curie tail below 5 K. For $0.1 \leq x < 0.9$, χ increases with decreasing temperature down to 2 K, but below 10 K, the deviation from Curie−Weiss behavior results in a reduction in the expected susceptibility. Conversely, $Ba_2Nd_{0.10}Mn_{0.90}MoO_6$ and $Ba_2Nd_{0.05}Mn_{0.95}MoO_6$ both show a small divergence between fc and zfc data when cooled below 5 K. These two compositions also show a small maximum in the zfc data indicative of a partial loss of moment due to antiferromagnetic correlations.

Fits of the data to the Curie−Weiss law for $T > 150$ K show that the Weiss constant, θ, is negative for all compositions,

indicating that the dominant interactions in these samples are antiferromagnetic. The magnitude of θ initially decreases across the series with increasing Mn content up to $x \approx 0.5$, as shown in Figure 6. When the Mn content was increased further, the magnitude of θ increases to a maximum of −85(2) K for the x = 1 end member. The Curie constant, C, also increases on increasing the Mn content across the series and is shown in Figure 6. This variation in the values of C agrees with that expected for Mn^{2+} substituting for Nd^{3+}, and the associated oxidation of Mo^{5+} to Mo^{6+} such that the stoichiometry of these compounds can be represented as $Ba_2Nd^{3+}_{1-x}Mn^{2+}_xMo^{5+}_{1-x}Mo^{6+}_xO_6$.

When $Ba_2Nd_{0.10}Mn_{0.90}MoO_6$ was cooled from 15 to 1.5 K, additional Bragg peaks appear that are systematically absent in the space group $Fm\bar{3}m$, as shown in Figure 7. The strong temperature dependence of these reflections at large d-spacings shows that these are indicative of a transition to a magnetically ordered state. These additional peaks can be indexed using a cubic magnetic cell with $a_{mag} = 2a_{nuc}$, indicative of long-range antiferromagnetic ordering with a propagation vector of $\mathbf{k}$ = (1/2, 1/2, 1/2). These magnetic peaks are appreciably broader than the nuclear Bragg peaks, suggesting that the magnetic ordering occurs over a shorter length scale than the atomic ordering. Modeling a finite moment on the Nd and Mo cations did not improve the quality of fit; therefore, these moments were fixed to have a zero value. The Rietveld refinement used a calculated form factor for Mn^{2+}.[19] A preliminary Rietveld refinement against the low temperature data was performed using the collinear magnetic structure proposed[13] for Ba_2MnMoO_6 and shown in Figure 8a, as a starting model. This resulted in the reasonable quality of fit shown in Figure 8b, with $\chi^2 = 6.31$, $R_{wp} = 6.75$, and a refined magnetic moment of 3.7(3) μ_B per Mn ion. An alternative magnetic model was then considered where the dominant magnetic exchange pathway between Mn ions was proposed to be the linear Mn−O−Mo−O−Mn interaction. Considering these interactions enables the Mn lattice to be viewed as four interpenetrating sublattices, as previously highlighted by Anderson.[20] The Mn ions on each of these sublattices can be considered to order in a collinear fashion as a G-type antiferromagnet. If each of these sublattices has the Mn moments orientated along one of the four different $\langle 111 \rangle$ directions, a magnetic structure containing fully spin-compensated tetrahedra and in which all the nearest neighbor interactions are identical can be constructed. This model and the resultant fitted refinement are shown in Figure 8 and resulted in an improvement agreement with the observed data, $\chi^2 = 5.99$, $R_{wp} = 6.58$, and a refined moment of 4.1(2) μ_B per Mn. The peak intensities of the two different magnetic models are compared with the observed intensities in Table 3.

■ DISCUSSION

A solid solution of cation-ordered perovskite phases exists between the tetragonal Ba_2NdMoO_6 and the cubic Ba_2MnMoO_6. The tetragonal distortion in the Nd-rich compounds of the series $Ba_2Nd_{1-x}Mn_xMoO_6$ is manifested in the Mo−O−Mn/Nd angle from 180°. This is progressively diminished with increasing x, and compositions containing 40% or more Mn display cubic symmetry. For increasing doping levels, the mean Nd/Mn−O distance is reduced as expected due to the smaller size of the Mn cation compared to Nd^{3+}. There is also a slight reduction in the size of the MoO_6 octahedra indicating a reduction in the effective radius of the molybdenum cation, suggesting that the oxidation state is being

Table 1. Structural Data Derived from Rietveld Refinement against Neutron or X-ray Diffraction Data

x	T (K)	space group	R_{wp}	χ^2	a (Å)	c (Å)	V (Å³)^c	Mo–O (Å)	Nd/Mn–O (Å)
0.05	298	$I4/m$	13.3	3.07	6.00180(11)	8.5504(2)	616.00(3)	1.85(2) × 4	2.41(2) × 4
								1.98(3) × 2	2.30(3) × 2
0.10^d	298	$I4/m$	3.15	3.54	5.99854(6)	8.5304(2)	613.87(2)	1.9541(12) × 4	2.3047(12) × 4
								1.955(2) × 2	2.311(2) × 2
0.10^d	15	$I4/m$	3.64	7.78	5.96596(7)	8.5653(2)	609.73(2)	1.951(2) × 4	2.308(2) × 4
								1.984(2) × 2	2.298(2) × 2
0.10^d	1.5	$I4/m$	3.66	7.83	5.96598(7)	8.5651(2)	609.71(2)	1.950(2) × 4	2.309(2) × 4
								1.986(2) × 2	2.297(2) × 2
0.20^d	298	$I4/m$	2.13	3.50	5.9908(2)	8.4650(5)	607.60(2)	1.925(5) × 4	2.319(5) × 4
								2.014(11) × 2	2.219(11) × 2
0.30^d	298	$I4/m$	4.15	9.27	5.9724(3)	8.4304(7)	601.41(3)	1.940(4) × 4	2.287(4) × 4
								1.970(8) × 2	2.245(8) × 2
0.30^d	15	$I4/m$	5.85	18.1	5.9535(4)	8.4088(10)	596.09(5)	1.943(6) × 4	2.285(6) × 4
								1.966(11) × 2	2.238(11) × 2
0.30^d	1.5	$I4/m$	5.87	18.2	5.9539(4)	8.4084(10)	596.14(5)	1.945(6) × 4	2.283(6) × 4
								1.964(11) × 2	2.241(11) × 2
0.40	298	$Fm\bar{3}m$	12.88	2.80	8.4009(2)		592.89(5)	2.09(8) × 6	2.11(8) × 6
0.50^d	298	$Fm\bar{3}m$	3.68	7.14	8.36201(13)		584.70(3)	1.9417(8)	2.2393(8) × 6
0.50^d	15	$Fm\bar{3}m$	4.17	5.28	8.3377(2)		579.62(3)	1.9342(9)	2.2346(9) × 6
0.50^d	1.5	$Fm\bar{3}m$	4.20	5.34	8.3375(2)		579.57(3)	1.9340(9)	2.2347(9) × 6
0.60	298	$Fm\bar{3}m$	14.37	3.67	8.3210(4)		576.13(8)	1.98(2)	2.18(2) × 6
0.70^d	298	$Fm\bar{3}m$	4.02	7.47	8.2828(2)		568.24(3)	1.9326(9)	2.2088(9) × 6
0.80	298	$Fm\bar{3}m$	14.18	3.70	8.2472(2)		560.94(4)	1.919(8)	2.204(8) × 6
0.90^d	298	$Fm\bar{3}m$	4.82	12.0	8.20686(8)		552.75(2)	1.9320(11)	2.1714(11) × 6
0.90^d	15	$Fm\bar{3}m$	5.71	13.8	8.19029(9)		549.41(2)	1.9284(11)	2.1668(11) × 6
0.90^d	1.5	$Fm\bar{3}m$	6.62	6.03	8.18876(9)		549.10(2)	1.9247(12)	2.1696(12) × 6
0.95	298	$Fm\bar{3}m$	13.54	3.24	8.19281(12)		549.92(3)	1.960(6)	2.136(6) × 6

^{a}$I4/m$ positions: Ba 1/4, 1/4, 1/4; Mo 0, 0, 1/2; Nd/Mn 0, 0, 0; O(1) 0, 0, z; O(2) x, y, 0. ^{b}$Fm\bar{3}m$ positions: Ba 1/4,1/4, 1/4; Mo 1/2, 1/2, 1/2; Nd/Mn 0, 0, 0; O(1) x, 0, 0. ^{c}Volumes for tetragonal compositions are reported as (V_{tet} × 2) to ease comparison with the cubic phases. ^{d}From refinements against neutron powder diffraction data.

Table 2. Magnetic Parameters Derived from Curie−Weiss Fits to the Susceptibility Data in the Temperature Range of $300 \geq T \geq 150$ (K)

x	θ (K)	C (cm³ K·mol⁻¹)	C_{calc} (cm³ K·mol⁻¹)
0	−51.6(8)	1.802(6)	2.01
0.05	−56(4)	2.13(3)	2.13
0.10	−47(4)	2.08(3)	2.24
0.20	−49(5)	2.33(5)	2.25
0.30	−40.3(11)	2.491(11)	2.72
0.40	−32(3)	2.83(3)	2.96
0.50	−24(2)	2.97(2)	3.19
0.60	−23.8(14)	2.94(2)	3.43
0.70	−26(2)	3.55(3)	3.66
0.80	−57(2)	4.37(4)	3.90
0.90	−51(2)	4.09(4)	4.13
0.95	−72(2)	4.38(4)	4.25
1	−85(2)	4.61(4)	4.38

C_{calc} was predicted using the moment from the full spin and orbital contribution from Nd^{3+} ($^4I_{9/2}$) and spin-only values from Mo^{5+} and high spin Mn^{2+} thus:

$$\mu = \left((1-x)[\mu(Nd^{3+})]^2 + (1-x)[\mu(Mo^{5+})]^2 + x[\mu(Mn^{2+})]^2 \right)^{1/2}$$

$$= ((1-x)[g(J_{Nd3+}(J_{Nd3+}+1))^{1/2}]^2 + (1-x)[g(S_{Mo5+}(S_{Mo5+}+1))^{1/2}]^2 + x[g(S_{Mn2+}(S_{Mn2+}+1))^{1/2}]^2)^{1/2}$$

increased from that of Mo^{5+} observed in Ba_2NdMoO_6. The X-ray diffraction data are insensitive to the displacements of the oxide anions due to the presence of the dominant scattering cations Ba, Nd, and Mo. Consequently, there are large standard deviations associated with the metal−oxide bond lengths derived from X-ray diffraction data.

The unit cell is close to metrically cubic in $Ba_2Nd_{0.80}Mn_{0.20}MoO_6$ and $Ba_2Nd_{0.70}Mn_{0.30}MoO_6$, but neutron diffraction reveals that the crystal symmetry in these two compounds is actually tetragonal due to rotation of the MO_6 octahedra about a 4-fold axis. Unlike the Ba_2NdMoO_6 parent phase, none of these compounds undergo a distortion to triclinic symmetry on cooling, and none show a significant distortion in the MoO_6 octahedra that drives this transition in Ba_2NdMoO_6 and Ba_2SmMoO_6. A study of the effect of replacement Nd^{3+} with the smaller Y^{3+} cation in the series $Ba_2Nd_{1-x}Y_xMoO_6$ has shown that the z-out distortion of the MoO_6 octahedra can persist in doped phases with occupational cation disorder.[21] In $Ba_2Nd_{0.90}Y_{0.10}MoO_6$, the distortion increases with decreasing temperature but does not reach the same magnitude as in Ba_2NdMoO_6, and the tetragonal symmetry is maintained to 2 K. Increased Y doping reduces the size of the distortion further, until it is eliminated for a composition of $Ba_2Nd_{0.65}Y_{0.35}MoO_6$. We show here that the MoO_6 distortion is eliminated as a much faster function of Mn doping than the equivalent substation with Y^{3+}. Both doping systems have a similar size mismatch, as illustrated by the fact that the both systems form cubic phases around $Ba_2Nd_{0.60}M_{0.40}MoO_6$. The greater ability of Mn doping to
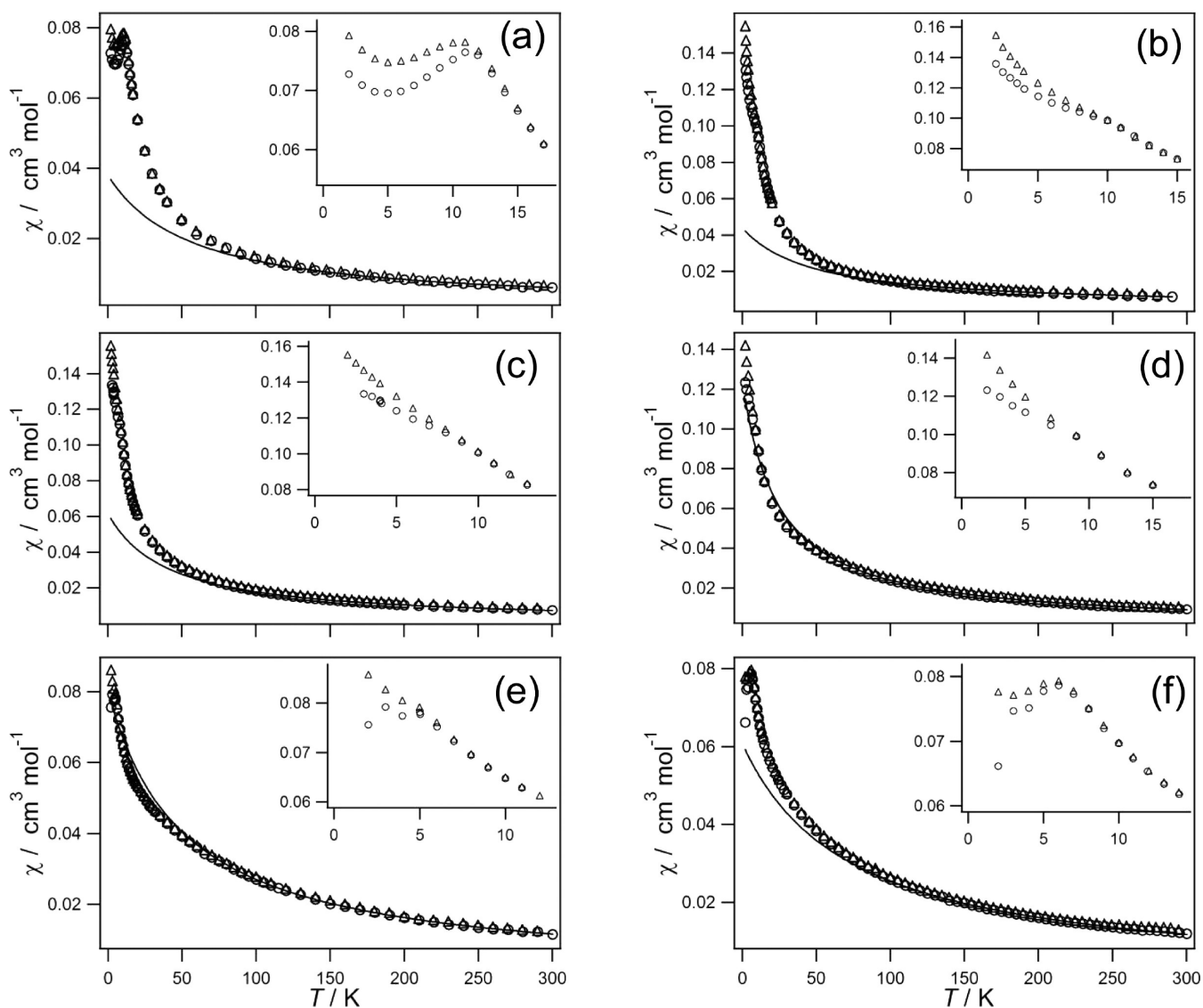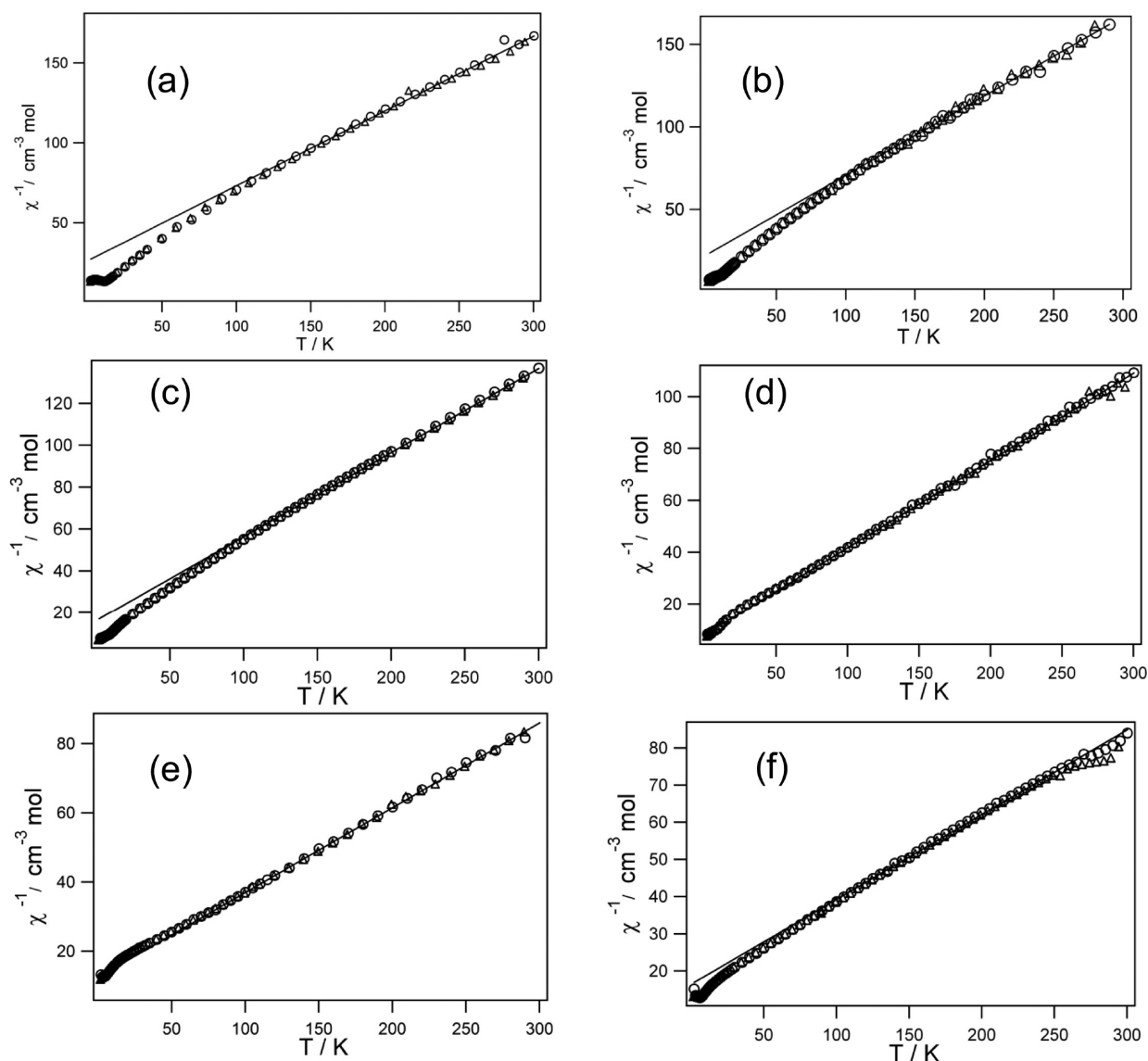
Figure 4. Depictions of *dc*-susceptibility of (a) $Ba_2Nd_{0.95}Mn_{0.05}MoO_6$, (b) $Ba_2Nd_{0.90}Mn_{0.10}MoO_6$, (c) $Ba_2Nd_{0.70}Mn_{0.30}MoO_6$, (d) $Ba_2Nd_{0.50}Mn_{0.50}MoO_6$, (e) $Ba_2Nd_{0.10}Mn_{0.90}MoO_6$, and (f) $Ba_2Nd_{0.05}Mn_{0.95}MoO_6$ measured after cooling the sample in zero applied field (circles) or in the measuring field of 1000 G (triangles). The black line is a fit to the Curie−Weiss law for $T \geq 150$ K. The insets show the low temperature data.

quench the MoO_6 distortion arises from the redox activity of manganese, and this is investigated using magnetic measurements.

Magnetic susceptibility measurements indicate that Curie−Weiss behavior persists at high temperatures for all compositions. The large negative Weiss constants are indicative of antiferromagnetic interactions. Ba_2NdMoO_6 shows a clear maximum in the susceptibility at 15 K due to the onset of long-range antiferromagnetic order.[10] With the exception of $Ba_2Nd_{0.95}Mn_{0.05}MoO_6$, none of the other compounds in the series show a sharp decrease in susceptibility indicative of spin cancellation through the bulk material. Instead, only a small deviation from Curie−Weiss behavior is observed, at temperatures much lower than the strength of the magnetic interactions indicated by the Weiss constants. Low temperature neutron diffraction data collected from $Ba_2Nd_{0.90}Mn_{0.10}MoO_6$ confirm the absence of long-range magnetic order, even at dopant levels well below the percolation limit for a face-centered cubic lattice of 0.195.[22] Long range magnetic order is

often observed in cation-ordered double perovskites where distortions from cubic symmetry lift the degeneracy of the interactions and so stabilize an ordered antiferromagnetic ground state.[23] In the related *fcc* rock salt structure of MnO the magnetic ordering transition is coupled with a structural distortion that partially alleviates the frustration.[24] The high resolution neutron diffraction data show that the Mn-rich compositions in the series $Ba_2Nd_{1-x}Mn_xMoO_6$ retain cubic symmetry to 1.5 K and so the frustration inherent in the *fcc* lattice is retained.

The dependence of the Curie constant on the composition indicates that manganese is doped into the lattice as Mn^{2+} with a corresponding oxidation of molybdenum to Mo^{6+}. Trial refinements indicating that the actual stoichiometries were within 1% of the target compositions show that the charge balance on substituting Mn^{2+} for Nd^{3+} cannot be accounted for by the formation of oxygen vacancies in this system. More sensitive, local probes such as NMR have been used to study related compounds and shown that disorder can exist at a level

Figure 5. Inverse *dc*-susceptibility of (a) $Ba_2Nd_{0.95}Mn_{0.05}MoO_6$, (b) $Ba_2Nd_{0.90}Mn_{0.10}MoO_6$, (c) $Ba_2Nd_{0.70}Mn_{0.30}MoO_6$, (d) $Ba_2Nd_{0.50}Mn_{0.50}MoO_6$, (e) $Ba_2Nd_{0.10}Mn_{0.90}MoO_6$, and (f) $Ba_2Nd_{0.05}Mn_{0.95}MoO_6$ measured after cooling the sample in zero applied field (circles) or in the measuring field of 1000 G (triangles). The black line is a fit to the Curie−Weiss law for $T \geq 150$ K.

below the detection limits of diffraction.[5] We note that the changes in the Curie constant as a function of composition are sufficiently large that if these arose from oxide non-stoichiometry then the neutron diffraction data would readily detect this concentration of vacancies. It is expected that, like the two end compositions, the members of this solid solution behave as localized electron systems, and this is confirmed by rudimentary room temperature resistance measurements.

In Ba_2NdMoO_6, the observed distortion reduces the electronic energy associated with the Mo^{5+}, t_{2g}^1 configuration. The absence of such a distortion in $Ba_2Nd_{1−x}Mn_xMoO_6$ for $x \geq 0.1$ can be rationalized with reference to the valence disorder introduced with Mn doping; the presence of the Mn^{2+}/Mo^{6+} cation pair introduces mixed valence onto the Mo site and partially removes the electronic driver for distortion. The introduction of manganese cations also disrupts crystallographic ordering of a distortion due to the local strain fields that will arise from the replacement of Nd^{3+} with the smaller Mn^{2+} and from the size differences between Mo^{5+} and Mo^{6+}.

Although all compositions show net antiferromagnetic interactions in the Curie−Weiss temperature domain, the strength of these interactions goes through a minimum at $x \sim$ 0.5. The initial decrease in $|\theta|$ with the introduction of manganese into the structure can be attributed to disruption of the superexchange pathways within the lattice arising from the partial oxidation of $S = 1/2$ Mo^{5+} to diamagnetic Mo^{6+}. Additionally, the coupling between the half-filled e_g orbitals of Mn^{2+} and the empty e_g orbitals of Mo^{5+} (via σ overlap with a bridging O 2p orbital) is predicted to give ferromagnetic coupling between the Mn^{2+} and Mo^{5+} cations. This ferromagnetic interaction is in competition with the anti-ferromagnetic exchange between Mo^{5+} and Nd^{3+} and so will lead to a partial cancellation of the net coupling.

This compositional series has the most disordered distribution of octahedrally coordinated cations for the composition $Ba_2Nd_{0.50}Mn_{0.50}MoO_6$. This compound contains a disordered 50:50 distribution of Nd^{3+}/Mn^{2+} on one crystallographic site and a 50:50 mixture of Mo^{5+}/Mo^{6+} cations on the other octahedrally coordinated site. The disorder is
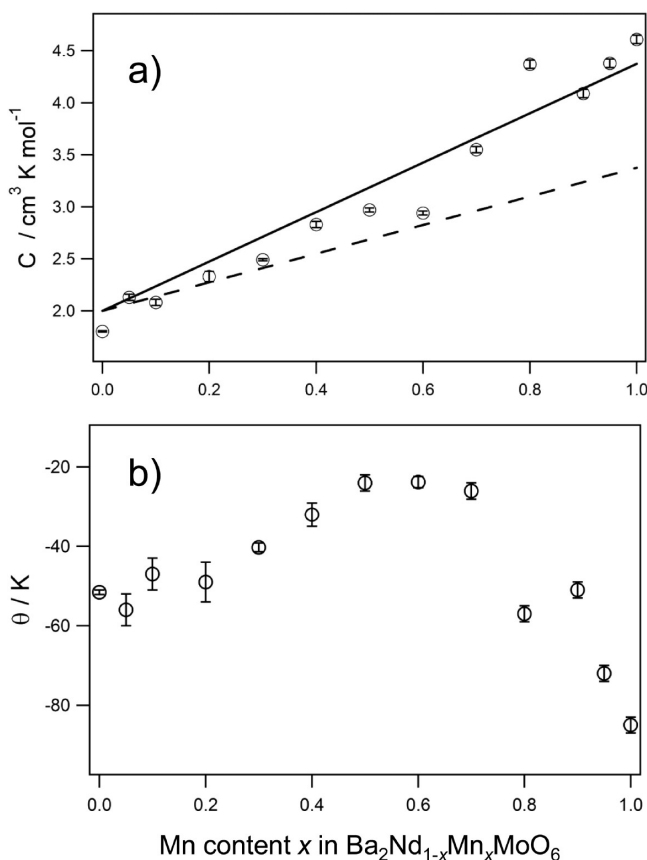
Figure 6. Variation of (a) the Curie constant, C, and (b) the Weiss constant, θ, with increasing Mn content, x, in the solid solution $Ba_2Nd_{1-x}Mn_xMoO_6$. Error bars represent one estimated standard deviation. The expected variations in C for doping with Mn^{2+} or Mn^{3+} are shown by the solid and broken lines, respectively. These were calculated assuming high-spin, spin-only moments for Mn^{2+}, Mn^{3+}, and Mo^{5+}, and a full orbital contribution for Nd^{3+} such that the solid and dashed lines correspond to moments given by $\mu = ((1 - x)[\mu(Nd^{3+})]^2 + (1 - x)[\mu(Mo^{5+})]^2 + x[\mu(Mn^{2+})]^2)^{1/2}$ and $\mu = ((1 - x)[\mu(Nd^{3+})]^2 + [\mu(Mn^{2+})]^2 + x[\mu(Mn^{3+})]^2)^{1/2}$, respectively.

reflected in the susceptibility data that show the magnitude of the net interaction is reduced with increasing Mn content up to 50% Mn substitution. Further increases in Mn^{2+} content result in an increase in $|\theta|$ as the superexchange interaction becomes dominated by the antiferromagnetic interaction between Mn^{2+} cations through intermediate Mo^{6+} cations.

The most Mn-rich compositions show a maximum in the zero-field cooled data that give an indication of possible antiferromagnetic ordering. Although the susceptibility data collected from $Ba_2Nd_{0.10}Mn_{0.90}MoO_6$ shown in Figure 4e indicate only a small deviation between fc and zfc data at ~5 K, which corresponds to a frustration index $f = ((|\theta|)/T_N) \approx 10.[25]$ Despite this, the neutron diffraction measurements at 1.5 K show intense Bragg peaks arising from long-range magnetic ordering. The propagation vector $\mathbf{k} = (1/2, 1/2, 1/2)$ indicates a doubling of the unit cell along each axis and is consistent with long-range antiferromagnetic order. This expansion results in a magnetic cell that contains 32 Mn sites. Initially, the magnetic model proposed for Ba_2MnMoO_6 was used as a basis for modeling the magnetic scattering.[13] This provides a reasonable fit to the data, but when the model was considered, neighboring moments situated on the vertices of equilateral triangles were found to have a mixture of both ferro- and antiferromagnetic
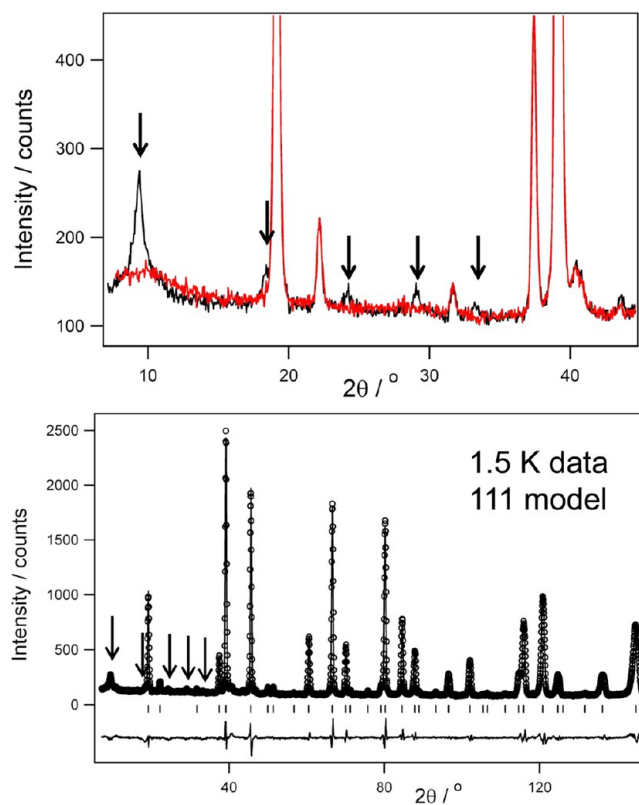

Figure 7. a) High d-spacing portion of the neutron diffraction profiles collected from $Ba_2Nd_{0.10}Mn_{0.90}MoO_6$ at temperatures of 15 K (red line) and 1.5 K (black line). Arrows indicate the position of magnetic scattering that is observed at 1.5 K but absent from the 15 K data set. (b) Full profile fitted with the noncollinear magnetic spin structure and cubic nuclear structure.

interactions. As there is no deviation from cubic symmetry in this compound, this mixture of interactions implies that different magnetic coupling exists between ion pairs that are symmetrically identical. The shortest distance between Mn^{2+} cations is $a/\sqrt{2} = 5.8$ Å, as shown in Figure 9. However, superexchange occurs via overlap of the orbitals between Mn−O−Mo−O−Mn rather than by a direct through-space interaction. If there is no significant contribution from direct π overlap between the O 2p orbitals, then the cubic symmetry of the structure means that there is the same degree of overlap between the nearest neighboring Mn−Mn at a distance of 5.8 Å as there is between the next-nearest neighbors. Both of these interactions have the same through-bond distance of 8.2 Å, as illustrated in Figure 9. The π-superexchange interaction involving the e_g orbitals of the cations and the oxygen p_y and p_x orbitals is similarly equivalent between Mn^{2+} nearest neighbors and next-nearest neighboring Mn^{2+} centers.

Alternative magnetic models where the dominant antiferromagnetic exchange pathways were the next-nearest neighbor, linear Mn−O−Mo−O−Mn interactions were therefore considered. The only model that is consistent with both the observed scattering and the cubic symmetry contains the four neighboring spins situated on each tetrahedron orientated along each one of the four distinct $\langle 111 \rangle$ crystallographic directions, with next-nearest neighbor spins orientated antiferromagnetically. Using this model resulted in a slight improvement to the quality of fit and an increased Mn moment of 4.1(2) μ_B. This moment in agreement with the value of
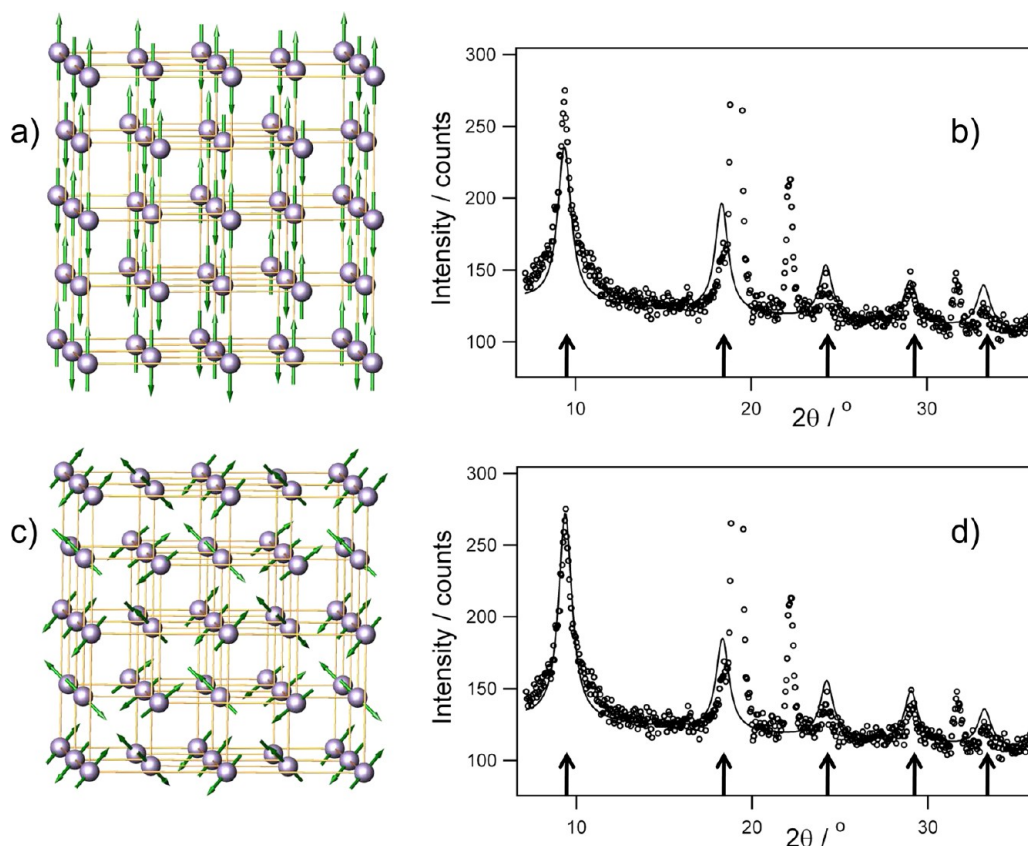
Figure 8. (a) Linear configuration of spins proposed[13] for Ba_2MnMoO_6 used as the basis of initial refinement of the magnetic structure of $Ba_2Nd_{0.10}Mn_{0.90}MoO_6$. (b) The neutron data observed at 1.5 K are represented as circles and the purely magnetic Bragg intensity arising from the model shown in (a) is shown as a solid black line. Arrows indicate the peaks that are purely magnetic in origin; no contribution from the nuclear structure has been included in this profile. (c) Alternative model proposed for the magnetic structure of $Ba_2Nd_{0.10}Mn_{0.90}MoO_6$ and (d) the fitted neutron diffraction pattern resulting from refinement of this magnetic model. The improved agreement between the magnetic model and the observed magnetic Bragg peaks is evident from comparing the better agreement in (d) compared to (b).

Table 3. Peak Intensities for the Two Different Magnetic Models

magnetic peak	int$_{obs}$	int$_{calc}$ [collinear model]	int$_{calc}$ [111 model]
(111)	199	177	223
(311)	15.2	28.1	24.1
(331)	24.4	30.1	32.9
(511), (333)	30.9	29.5	36.7
(531)	29.6	59.1	53.2

4.04(8) μ_B observed in Ba_2MnMoO_6 by Martínez-Lope et al. for high-spin Mn^{2+}, with the moment slightly lowered by covalency effects.[26] This model is consistent with the cubic symmetry of the phase as all nearest neighbor exchange interactions are identical. We note that the almost complete ordering of the magnetic moments implied by the high value of the refined moment per Mn^{2+} is not indicated by the susceptibility measurements. Such strong antiferromagnetic order would be anticipated to lead to significant reduction in the magnetization due to cancellation of moments. The contradiction between the long-range antiferromagnetism observed using neutron scattering at 1.5 K and the apparent absence of a Néel transition in the bulk magnetization data demands further explanation. To this end, detailed investigations of the low-temperature magnetic state of Ba_2MnMoO_6 and $Ba_2Nd_{0.10}Mn_{0.90}MoO_6$ are underway.

■ CONCLUSIONS

The solid solution $Ba_2Nd_{1-x}Mn_xMoO_6$ has been prepared for all values of x. The Curie−Weiss magnetic behavior is consistent with the introduction of Mn^{2+} and the associated oxidation of Mo^{5+} to diamagnetic Mo^{6+}. All these compounds contain antiferromagnetic interactions, which are most significant for the compounds toward each end of the series. Despite this, each of the compounds only shows a small deviation from Curie−Weiss behavior at temperatures of 10 K or below. The tetragonal distortion observed in Ba_2NdMoO_6 is only observed for $x \leq 0.3$, and this is manifested as a tilting of the oxide octahedra within a cell which is metrically close to cubic. The long-range antiferromagnetic order of the Ba_2NdMoO_6 end-member is rapidly suppressed by the introduction of chemical disorder on the Nd/Mn site and the simultaneous presence of mixed valence on the Mo^{5+}/Mo^{6+} position. The tetragonal symmetry is maintained to 1.5 K for $Ba_2Nd_{0.70}Mn_{0.30}MoO_6$. For $x \geq 0.5$, all compositions show no deviation from cubic symmetry, even when cooled to 1.5 K. $Ba_2Nd_{0.10}Mn_{0.90}MoO_6$ undergoes a phase transition to an antiferromagnetically ordered phase when cooled to 1.5 K, which is best modeled using a noncollinear magnetic structure, with spins aligned along each of the four $\langle 111 \rangle$ type directions.
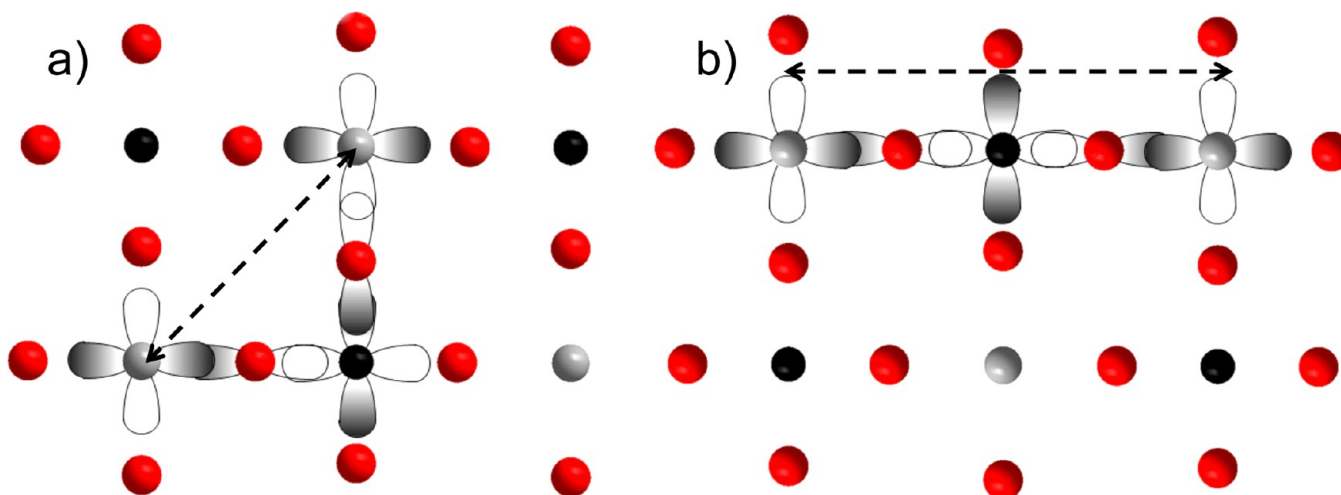
Figure 9. Shows the σ-superexchange pathway between paramagnetic Mn^{2+} centers that are either nearest neighbors (a) or next-nearest neighbors (b), involving the same degree of orbital overlap between the 3d orbitals of the Mn^{2+} and Mo^{6+} cations and the $2p_z$ orbitals of the oxide anions. Mn^{2+}, Mo^{6+}, and O^{2-} are illustrated by gray, black, and red spheres, respectively. The through-space distance between Mn^{2+} cations is much shorter for nearest neighbors, at a distance of 5.8 Å, indicated by the arrow in (a), compared to the next-nearest neighbors at a distance of 8.2 Å, as indicated in (b).

■ ASSOCIATED CONTENT

Ⓢ Supporting Information

Crystallographic coordinates derived from Rietveld refinement against neutron powder diffraction data. This material is available free of charge via the Internet at http://pubs.acs.org.

■ AUTHOR INFORMATION

Corresponding Author

*E-mail: edmund.cussen@strath.ac.uk. Tel.: +44 141 548 2797.

Present Address

†ISIS Neutron and Muon Source, STFC Rutherford Appleton Laboratory, Harwell Science and Innovation Campus, Didcot, Oxfordshire OX11 0QX, United Kingdom.

Notes

The authors declare no competing financial interest.

■ ACKNOWLEDGMENTS

■ REFERENCES

(1) Raveau, B.; Maignan, A.; Martin, C.; Hervieu, M. *Chem. Mater.* **1998**, *10*, 2641.

(2) Hotta, T.; Malvezzi, A. L.; Dagotto, E. *Phys. Rev. B* **2000**, *62*, 9432.

(3) Clarke, S. J.; Fowkes, A. J.; Harrison, A.; Ibberson, R. M.; Rosseinsky, M. J. *Chem. Mater.* **1998**, *10*, 372.

(4) Greedan, J. E. In *Functional Oxides*; Bruce, D. W., O'Hare, D., Walton, R. I., Eds.; John Wiley & Sons, Ltd.: Chichester, U.K., 2010, p 41−109.

(5) Aharen, T.; Greedan, J. E.; Bridges, C. A.; Aczel, A. A.; Rodriguez, J.; MacDougall, G.; Luke, G. M.; Imai, T.; Michaelis, V. K.; Kroeker, S.; Zhou, H. D.; Wiebe, C. R.; Cranswick, L. M. D. *Phys. Rev. B* **2010**, *81*, 224409.

(6) de Vries, M. A.; McLaughlin, A. C.; Bos, J. W. G. *Phys. Rev. Lett.* **2010**, *104*, 177202.

(7) Wallace, T. K.; Colman, R. H.; McLaughlin, A. C. *Phys. Chem. Chem. Phys.* **2013**, *15*, 8672.

(8) Mclaughlin, A. C. *Phys. Rev. B* **2008**, *78*, 132404.

(9) Cussen, E. J.; Cameron, W. J. *J. Mater. Chem.* **2010**, *20*, 1340.

(10) Cussen, E. J.; Lynham, D. R.; Rogers, J. *Chem. Mater.* **2006**, *18*, 2855.

(11) McLaughlin, A. C.; de Vries, M. A.; Bos, J. W. G. *Phys. Rev. B* **2010**, *82*, 094424.

(12) Coomer, F. C.; Cussen, E. J. *J. Phys.: Condens. Matter* **2013**, *25*, 082202.

(13) Martinez-Lope, M. J.; Alonso, J. A.; Casais, M. T. *Z. Naturforsch., B: Chem. Sci.* **2003**, *58*, 571.

(14) Azad, A. K.; Eriksson, S.-G.; Ivvanov, S. A.; Mathieu, R.; Svedlindh, S. P.; Eriksen, J.; Rundlof, H. *J. Alloys Compd.* **2004**, *364*, 77.

(15) Lv, S. H.; Liu, X. J.; Li, H. P.; Wu, Z. J.; Meng, J. A. *Comput. Mater. Sci.* **2010**, *49*, 266.

(16) Larson, A. C.; von Dreele, R. B. *General Structure Analysis System (GSAS)*; Los Alamos National Laboratories: Los Alamos, NM, 1990.

(17) Toby, B. H. *J. Appl. Crystallogr.* **2001**, *34*, 210.

(18) Glazer, A. M. *Acta Crystallogr.* **1972**, *B 28*, 3384.

(19) Brown, P. J. In *International Tables for Crystallography*, 4th ed.; Kluwer Academic Publishers: Dordrecht, The Netherlands, 1995; Vol. C, p 512.

(20) Anderson, P. W. *Phys. Rev.* **1950**, *79*, 705.

(21) Collins, O. M.; Cussen, E. J. *J. Solid State Chem.* **2013**, *200*, 215.

(22) Stauffer, D. *Phys. Rep.* **1979**, *54*, 1.

(23) Cussen, E. J. *J. Solid State Chem.* **2007**, *180*, 474.

(24) Goodwin, A. L; Tucker, M. G.; Dove, M. T.; Keen, D. A. *Phys. Rev. Lett.* **2006**, *96*, 047209.

(25) Greedan, J. E. *J. Mater. Chem.* **2001**, *11*, 37.

(26) Tofield, B. C.; Fender, B. E. F. *J. Phys. Chem. Solids* **1970**, *31*, 2741.